Journal of Computational Physics 326 (2016) 56–75

Contents lists available at ScienceDirect

Journal of Computational Physics

www.elsevier.com/locate/jcp

A blended continuous–discontinuous finite element method for solving the multi-fluid plasma model

E.M. Sousa *, U. Shumlak

Aerospace and Energetics Research Program, University of Washington, Seattle, WA, United States

ARTICLE INFO

Article history:
Received 8 January 2016
Received in revised form 16 June 2016
Accepted 27 August 2016
Available online 31 August 2016

Keywords:
High-order
Discontinuous Galerkin finite element method
Continuous Galerkin finite element method
Implicit–explicit (IMEX) scheme
Multi-fluid plasma model

ABSTRACT

The multi-fluid plasma model represents electrons, multiple ion species, and multiple neutral species as separate fluids that interact through short-range collisions and long-range electromagnetic fields. The model spans a large range of temporal and spatial scales, which renders the model stiff and presents numerical challenges. To address the large range of timescales, a blended continuous and discontinuous Galerkin method is proposed, where the massive ion and neutral species are modeled using an explicit discontinuous Galerkin method while the electrons and electromagnetic fields are modeled using an implicit continuous Galerkin method. This approach is able to capture large-gradient ion and neutral physics like shock formation, while resolving high-frequency electron dynamics in a computationally efficient manner. The details of the Blended Finite Element Method (BFEM) are presented. The numerical method is benchmarked for accuracy and tested using two-fluid one-dimensional soliton problem and electromagnetic shock problem. The results are compared to conventional finite volume and finite element methods, and demonstrate that the BFEM is particularly effective in resolving physics in stiff problems involving realistic physical parameters, including realistic electron mass and speed of light. The benefit is illustrated by computing a three-fluid plasma application that demonstrates species separation in multi-component plasmas.

1. Introduction

Plasmas can be represented by a hierarchy of models; the more general the model, the higher the computational cost. In plasma simulations it is therefore important to devise methods that maximize computational efficiency, while capturing the desired physics.

In kinetic theory, each constituent plasma species is represented by a probability distribution function $f(\mathbf{x}, \mathbf{v}, t)$ that depends on position, velocity, and time. The evolution of the distribution function is governed by the Boltzmann–Maxwell equation system. Solving the Boltzmann equation is computationally expensive due to the fact that the distribution functions occupy a six-dimensional phase space.

The two-fluid plasma model can be derived from the kinetic model by taking velocity moments [1], which reduces the six-dimensional space to three dimensions. Inherent in the derivation of the two-fluid model is the assumption of local thermodynamic equilibrium within each species, but not between different species. The governing equations for the two-fluid model are derived by taking the first three velocity moments of the Boltzmann equation for the electrons and for

* Corresponding author.
E-mail addresses: sousae@uw.edu (E.M. Sousa), shumlak@uw.edu (U. Shumlak).

http://dx.doi.org/10.1016/j.jcp.2016.08.044
0021-9991/

the ions. The zeroth moment describes the conservation of mass, the first moment describes the conservation of momentum, and the third moment describes the conservation of energy. The moments of the Boltzmann equation describe the evolution of the bulk properties of the plasma: density, momentum, and energy. In the simplest two-fluid description, the pressure is assumed to be isotropic and the heat flux is assumed to be negligible [1].

The magnetohydrodynamics (MHD) model, the most widely used plasma model, is derived from the two-fluid plasma model by neglecting the electron inertia (zero electron mass) and assuming the speed of light is much larger than any other speed in the system (infinite speed of light) [2]. As a consequence of neglecting the electron inertia, the electron momentum equation reduces to the generalized Ohm's law and the kinetic energy of the electrons is zero. By making these asymptotic assumptions, the physics of high frequency electromagnetic waves is ignored and the vacuum permittivity is effectively set to zero. This means that the displacement current term of Ampere's law is zero, and from Poisson's equation a zero permittivity implies that the electron and ion number density must always be equal, thereby enforcing charge neutrality. The MHD model is often further simplified to an ideal MHD model, which limits its applicability to high collisionality, small Larmor radius, and low resistivity regimes [3].

The two-fluid plasma model can be generalized to a multi-fluid plasma model that includes multiple ions and neutral species, where the mass, momentum, and energy of each species is evolved separately, and the species interact with each other through collisions and electromagnetic fields [4,5]. By separately evolving the constituent species, the multi-fluid plasma model is able to capture more generalized physics than MHD, but at a higher computational cost. The mass of the constituent species and their plasma parameters set the range of spatial and temporal scales. Since the multi-fluid plasma model does not make asymptotic assumptions about the speed of light, it captures more waves than MHD, including waves that propagate faster than the magnetosonic speed. This has been demonstrated for the two-fluid plasma model [1].

The characteristic speeds of the multi-fluid plasma model are the species' acoustic speeds and the speed of light, both of which can severely limit the time step size for the numerical time integration. In addition, the characteristic frequencies (plasma and cyclotron) need to be resolved to capture the full physics of the multi-fluid model.

For a given model, the partial differential equation (PDE) type informs the choice of numerical methods used to solve it. The multi-fluid plasma model is an inhomogeneous hyperbolic equation system and can be described by balance laws. Such equation systems can be solved using a variety of methods, including finite volume methods [6–8], continuous Galerkin finite element methods [9,10], and discontinuous Galerkin finite element methods [11–14].

Finite volume methods have been used extensively and differ depending on the technique used to evaluate fluxes. One type of finite volume method is the wave propagation method, which is second-order accurate and provides good resolution of shocks and discontinuities even when the initial conditions are smooth [6]. Other types of finite volume methods have been successfully applied to the MHD plasma model [15–17] and to the two-fluid plasma model [1,18]. Since the source terms in the PDEs cannot be directly incorporated into the calculation of the fluxes in the wave propagation method, the approach requires source splitting. As a result phase errors can be produced when the characteristic frequency is high compared to the frequency of information propagation [14].

Continuous Galerkin (CG) finite element methods have also been used for solving MHD [9] and extended MHD equations [10]. The CG method represents the solution variables within each element using polynomial basis functions. The order of the polynomial determines the spatial order of accuracy. The CG method enforces continuity of the solution across element boundaries, i.e. C^0 continuity. Some CG methods enforce C^1 continuity of the solution across element boundaries [9]. The CG method is particularly well suited for smooth solutions and offers the ability to compute solutions at high-order spatial accuracy on regular and unstructured grids [19–22]. With no dissipation, CG methods can be prone to dispersive errors and often require adding an artificial dissipation to damp high frequency oscillations [23]. The ideal multi-fluid plasma model has no physical source of dissipation, and thus using a CG method necessitates the introduction of artificial dissipation.

CG methods require the simultaneous solution of the global system of equations, which involves a matrix inversion. This feature allows CG to be coupled with an implicit time integration method with only minor modification. Plasma dynamics encompass a large range of timescales, which makes implicit time integration desirable. With implicit time integration, the solver is not subject to CFL (Courant–Friedrichs–Lewy) restrictions that limit time step size based on the fastest speed in the system. As two relevant plasma examples, in Ref. [24] an implicit method is applied together with a CG spatial discretization, and in Ref. [25] the hyperbolic MHD model is converted into parabolic equations in order to make them more amenable to multigrid and physics-based preconditioning that allow for fast Jacobian-free implicit time integration.

A numerical method that combines the shock capturing and conservation properties of finite volume methods with high-order accuracy and flux/source coupling of CG methods is the discontinuous Galerkin (DG) finite element method. The DG method was introduced in Ref. [26] for the study of two-dimensional neutron transport. Like the CG methods, DG methods represent the solution by a set of polynomial basis functions in each element; however, continuity of the solution is not enforced across the element boundaries. The DG method was expanded to solve non-linear equations in Ref. [11] who used it with total variation diminishing (TVD) Runge–Kutta time integration. Likewise the DG method has been applied to solve Navier–Stokes equations [27] on unstructured grids with linear, quadratic, and cubic elements [28–30].

In plasma simulations the DG method has been applied to the ideal MHD model [12,13,31], and to the Vlasov–Poisson equation system [32]. In Ref. [14] an extensive study of the DG method is applied to the two-fluid plasma model and explores the challenges associated with capturing the physical dispersion of the model. It is shown that the DG method is able to accurately capture physically expected high frequency oscillations using higher order discretizations without producing phase errors. A major benefit of the DG method is that it is remarkably robust in the presence of rapid oscillations while

simultaneously capturing discontinuity fronts. A drawback of the DG method is that with a polynomial basis function of degree p, the explicit time step size is limited by the CFL condition for the fastest wave to be less than $1/(2p-1)$ [33]. This can be extremely restrictive for problems that require high spatial accuracy. Using DG with implicit time integration can be challenging [34], this is because defining the Jacobian for a limited flux leads to a stiff matrix since small variations in the conserved variables can produce large changes in the flux. Reference [35] presents a complete two-fluid plasma model discretized using the DG method with an implicit time integrator; however, the non-linear Newton solver required for time advance does not always converge. This is due to the fact that regions that exhibit sharp gradients require limiters, which make the Jacobian for the non-linear solver ill-conditioned.

An ideal numerical method for the multi-fluid plasma model would have high-order accuracy, would be capable of capturing shocks, would provide good resolution of fast oscillations, and would not impose restrictive time step limitations. To that end, this paper presents a one-dimensional blended finite element method (BFEM) in which the electron fluid and the electromagnetic fields are represented using an implicit CG method, while all ions and neutral fluids are represented using an explicit DG method. This choice of blended discretization is informed by the physical properties of electrons, ions, neutrals, and fields.

Implicit–explicit (IMEX) methods have been used in the past for advection–diffusion problems where the implicit discretization is applied to parabolic diffusive source term and the explicit discretization is applied to the hyperbolic convective term [36]. IMEX methods have also been applied to geometry-induced stiffness [37], when a problem has complex geometry and consequently a broad range on mesh sizes. In our cases the stiffness comes from the electrons and electromagnetic fields that need to be solved everywhere in the domain and though the convective term. In the implicit–explicit scheme presented here is as if two separate problems exist, one advanced implicitly and the other explicitly and them both are coupled through the source term.

In many plasma configurations of interest, e.g. Z-pinches [38], tokamaks [39], stellarators [40], inertial confinement fusion capsules [41], the electron fluid and the electromagnetic fields may not have sharp gradients or discontinuities, which makes them suitable to being modeled with the CG method. Smooth solutions in the electron fluid and electromagnetic fields alleviate the need for limiters and enable the use of implicit time integration. Using the BFEM for the multi-fluid plasma model thus removes the strictest time step limitations associated with the speed of light, the electron acoustic speed, and the electron plasma and cyclotron frequencies. Shocks, which require limiters, only occur in ion and neutral fluids, and are efficiently captured with the DG method.

By coupling CG for the electrons and fields with DG for the ions and neutrals, the BFEM maintains high-order spatial accuracy, is able to resolve fast oscillations, efficiently captures shocks, and the implicit electron evolution relaxes the time step restrictions considerably by removing the most stringent limitations. This makes the BFEM for the multi-fluid plasma model more computationally efficient and robust than using a single type of finite element discretization.

This paper presents the development of a blended continuous–discontinuous finite element method, investigates its application to the multi-fluid plasma model. This method is particularly helpful in multiscale problems with disparate time-scales and where the fast dynamics does not play a vital role, nor is of much interest. Therefore, the fast dynamics is integrated using an implicit time integration to avoid very restrictive time-steps while the slow physics is integrated explicitly to capture the relevant aspects of the problem. The fast physics, which is unlikely to shock, is discretized using a continuous Galerkin finite element method and requires no limiters or flux calculations reducing the complexity of the numerical method. The slow dynamics is spatially discretized using a discontinuous Galerkin finite element method to capture shocks that may form in the solution. In summary the BFEM is designed to capture shocks for slow fluids while time-stepping over the fast dynamics fluids in problems where these two fluids are coupled throughout the computational domain. The paper is organized as follows: Section 2 describes the multi-fluid plasma model and the associated partial differential equation system. Section 3 introduces the BFEM implementation details and presents the continuous and discontinuous Galerkin portions of the method and their coupling. Section 4 presents numerical results for the two-fluid soliton problem and the electromagnetic shock tube problem. It also includes the application of the BFEM to a three-fluid plasma simulation of species separation [42] during the implosion of inertial confinement fusion capsules. Section 5 presents concluding remarks and opportunities for future work.

2. Multi-fluid plasma model

The multi-fluid plasma model [4] represents each species, e.g. electrons, ions, neutrals, as a separate fluid. The model allows for multiple ion and neutral species. Each fluid is described by its local mass density, momentum density, and total energy density. The evolution of these properties obeys underlying conservation laws. The motion of the electrically charged fluids generates and responds to electromagnetic fields, which are described by Maxwell's equations.

The equations that govern the evolution of the fluid properties of species α are derived by taking velocity moments of the Vlasov equation, where the nth moment is given by

$$m_\alpha \int \mathbf{v}^n \frac{\partial f_\alpha}{\partial t} d\mathbf{v} + m_\alpha \int \mathbf{v}^{n+1} \cdot \frac{\partial f_\alpha}{\partial \mathbf{x}} d\mathbf{v} + q_\alpha \int \mathbf{v}^n \left(\mathbf{E} + \mathbf{v} \times \mathbf{B}\right) \cdot \frac{\partial f_\alpha}{\partial \mathbf{v}} d\mathbf{v} = 0, \tag{1}$$

where $f_\alpha(\mathbf{x}, \mathbf{v})$ denotes the distribution function, m_α is the particle mass, and q_α is the charge. The electric and magnetic fields are $\mathbf{E}$ and $\mathbf{B}$.

Expressions for the conservation of mass, momentum, and total energy for each species are obtained from the first three moments, $n = \{0, 1, 2\}$, where a tensor contraction is performed for the second moment to give a scalar energy. The resulting equation system is the multi-fluid plasma model. Each fluid species α has a set of five moment equations,

$$\frac{\partial \rho_\alpha}{\partial t} + \nabla \cdot (\rho_\alpha \mathbf{u}_\alpha) = 0 \tag{2}$$

$$\frac{\partial \rho_\alpha \mathbf{u}_\alpha}{\partial t} + \nabla \cdot (\rho_\alpha \mathbf{u}_\alpha \mathbf{u}_\alpha + p_\alpha \mathcal{I}) = \frac{\rho_\alpha q_\alpha}{m_\alpha}(\mathbf{E} + \mathbf{u}_\alpha \times \mathbf{B}) \tag{3}$$

$$\frac{\partial \varepsilon_\alpha}{\partial t} + \nabla \cdot ((\varepsilon_\alpha + p_\alpha)\mathbf{u}_\alpha) = \frac{\rho_\alpha q_\alpha}{m_\alpha}\mathbf{u}_\alpha \cdot \mathbf{E}, \tag{4}$$

where ρ_α is the mass density, which is the product of the particle number density and particle mass, $\rho_\alpha = n_\alpha m_\alpha$, $\mathbf{u}_\alpha$ is the fluid velocity vector, p_α is the pressure, which is the product of the particle number density and temperature, $p_\alpha = n_\alpha T_\alpha$, $\mathcal{I}$ is the identity matrix, and ε_α is the total energy given by

$$\varepsilon_\alpha = \frac{p_\alpha}{\Gamma - 1} + \frac{1}{2}\rho_\alpha u_\alpha^2, \tag{5}$$

where Γ is the ratio of specific heats. Maxwell's equations govern the evolution of the electric and magnetic fields.

$$\frac{1}{c^2}\frac{\partial \mathbf{E}}{\partial t} - \nabla \times \mathbf{B} = -\mu_0 \sum_\alpha \frac{q_\alpha}{m_\alpha}\rho_\alpha \mathbf{u}_\alpha \tag{6}$$

$$\frac{\partial \mathbf{B}}{\partial t} + \nabla \times \mathbf{E} = 0 \tag{7}$$

$$\epsilon_0 \nabla \cdot \mathbf{E} = \sum_\alpha \frac{q_\alpha}{m_\alpha}\rho_\alpha \tag{8}$$

$$\nabla \cdot \mathbf{B} = 0 \tag{9}$$

where μ_0 and ϵ_0 are the vacuum permeability and permittivity, respectively, and $c = (\mu_0 \epsilon_0)^{-1/2}$ is the speed of light. Maxwell's equations are overdetermined with six scalar unknowns and eight equations. The two divergence expressions are analytically satisfied over time if they are initially satisfied, but computational round-off errors can produce fields that violate the divergence expressions. To clean the divergence errors, Maxwell's equations are cast in a purely hyperbolic form as described in Ref. [43].

$$\frac{\partial \mathbf{B}}{\partial t} + \nabla \times \mathbf{E} + \gamma \nabla \Psi = 0 \tag{10}$$

$$\frac{1}{c^2}\frac{\partial \mathbf{E}}{\partial t} - \nabla \times \mathbf{B} + \chi \nabla \Phi = -\mu_0 \sum_\alpha \frac{q_\alpha}{m_\alpha}\rho_\alpha \mathbf{u}_\alpha \tag{11}$$

$$\frac{1}{\chi}\frac{\partial \Phi}{\partial t} + \nabla \cdot \mathbf{E} = \sum_\alpha \frac{q_\alpha}{m_\alpha}\rho_\alpha \tag{12}$$

$$\frac{1}{\gamma c^2}\frac{\partial \Psi}{\partial t} + \nabla \cdot \mathbf{B} = 0 \tag{13}$$

Error correction potentials Φ and Ψ are introduced to propagate the divergence errors out of the computational domain. The divergence error propagation speeds are set by the dimensionless positive parameters χ and γ, which are set to values greater than one. Larger values better preserve the divergence constraints on the fields, and zero effectively eliminates any divergence corrections. The characteristic wave speeds for the purely hyperbolic Maxwell's equations are $\{\pm c, \pm \chi c, \pm \gamma c\}$.

The governing equations of the multi-fluid plasma model can be cast in balance law form as

$$\frac{\partial \mathbf{Q}}{\partial t} + \nabla \cdot \mathcal{F}(\mathbf{Q}) = \mathbf{S}(\mathbf{Q}), \tag{14}$$

where $\mathbf{Q}$ is the solution vector, $\mathcal{F}$ is the flux tensor and $\mathbf{S}$ is the source vector. The solution vector in Eq. (14) represents the union of the solution vector for electromagnetic field equations and the vector of the conserved variables for each fluid, e.g. electron fluid, ion fluid,..., such that $\mathbf{Q} = [\mathbf{Q}_{EM}, \mathbf{Q}_e, \mathbf{Q}_i, \ldots]$. The homogeneous version of Eq. (14) with $\mathbf{S} = 0$ is hyperbolic, meaning that the flux Jacobian, $\partial \mathcal{F}/\partial \mathbf{Q}$, is diagonalizable with real eigenvalues and has a complete set of eigenvectors. The source term in Eq. (14) depends only on $\mathbf{Q}$ and not on derivatives of $\mathbf{Q}$, such that $\mathbf{S}$ can be evaluated locally.

The eigenvalues of the flux Jacobian ($\partial \mathcal{F}/\partial \mathbf{Q}$) are the characteristic speeds of the multi-fluid equation system, and are combinations of the species' flow speeds, acoustic speeds, light speed, and divergence error propagation speeds. The eigen-

values of the source Jacobian ($\partial \mathbf{S}/\partial \mathbf{Q}$) are all purely imaginary [18,14] and the first three are $0, \pm i\omega_p$, where $\omega_p^2 = \sum_\alpha \omega_{p\alpha}^2$ and

$$\omega_{p\alpha} = \sqrt{\frac{\rho_\alpha q_\alpha^2}{\epsilon_0 m_\alpha^2}}, \tag{15}$$

which is the plasma frequency of the species α.

The imaginary eigenvalues of the source Jacobian indicate that dispersive behavior is physically expected and not necessarily a numerical artifact. This dispersion is due to the presence of a wide variety of plasma waves that result from the interaction of the charged fluids with the electromagnetic fields.

The characteristic timescales for the multi-fluid plasma model span a large range from extremely fast electromagnetic waves and electron response to much slower ion and neutral responses. The multi-fluid plasma model is mathematically stiff, which presents a challenge for numerical methods; explicit methods must resolve the shortest timescale, and implicit methods must invert a poorly conditioned matrix.

3. Blended finite element method

The stiffness introduced by the disparate timescales can be addressed by decomposing the multi-fluid plasma model according to physically expected temporal and spatial characteristics. The BFEM accomplishes this physics-based decomposition by modeling the ion and neutral fluids using a DG method with explicit Runge–Kutta time integration and modeling the electron fluid and the electromagnetic fields using a CG method with implicit time integration [44]. Since the fast moving electrons and the fields do not form spatial discontinuities, such as shocks, limiters are not needed and the Jacobian for a Newton solver is well-conditioned. This allows for larger time steps compared to an explicit method. The CFL constraint for explicit treatment of only the massive fluid species is less restrictive in this BFEM than in the case where all variables are evolved explicitly. Furthermore, the evolution of the ions and neutrals is often the goal of the simulation, so the temporal resolution provided by the explicit time steps is appropriate for these species. Source terms in the governing equations of the multi-fluid plasma model couple the fluids and fields, as described in Sec. 2. The BFEM computes the source terms in a manner that is consistent with both the CG and DG methods.

3.1. Continuous Galerkin finite element method

The finite element method discretizes the computational domain into elements and the solution is expanded within each element, Ω, in a series of polynomial basis functions. The order of the polynomials defines the spatial order of accuracy of the numerical method. The CG method enforces the solution to be continuous across element boundaries providing C^0 continuity. Continuity of derivatives across the element boundaries is not enforced [45].

The governing equations for the electron fluid and the electromagnetic fields of the multi-fluid plasma model are expressed by Eq. (14) where the solution vector is limited to $\mathbf{Q}^f = [\mathbf{Q}_{EM}, \mathbf{Q}_e]$. This subset of the governing equations accounts for the fast dynamics, denoted by the f superscript on the solution vector. The equation is then written as

$$\frac{\partial \mathbf{Q}^f}{\partial t} + \frac{\partial \mathcal{F}}{\partial \mathbf{Q}^f} \cdot \frac{\partial \mathbf{Q}^f}{\partial \mathbf{x}} = \mathbf{S}^f, \tag{16}$$

where $\partial \mathcal{F}/\partial \mathbf{Q}^f$ is the flux Jacobian. Since the flux $\mathcal{F}$ is a tensor of rank-2, $\mathcal{F}_{ij}$ in index notation, the flux Jacobian is a tensor of rank-3, $\mathcal{A}_{ijk} = \partial \mathcal{F}_{ki}/\partial Q_j^f$. Equation (16) can be expressed as

$$\frac{\partial Q_i^f}{\partial t} + \mathcal{A}_{ijk} \frac{\partial Q_j^f}{\partial x_k} = S_i, \tag{17}$$

where repeated indices in a term are summed, as usual in Einstein notation. The solution vector is expanded within each element using polynomial functions

$$\mathbf{Q}^f(t, x) = \sum_{j=1}^{m} \mathbf{q}_j(t) \psi_j(x), \tag{18}$$

where ψ_j are the spatial basis functions and $\mathbf{q}_j$ are the time-dependent coefficients. The f superscript is omitted from the temporal coefficients to simplify the notation. If Lagrange interpolation polynomials are used as the basis functions, $\mathbf{q}_j$ represent the values of the solution vector $\mathbf{Q}^f$ at each nodal location x^j. The Lagrange polynomials are defined as

$$\psi_j(x) = \prod_{k=1, k\neq j}^{m} \frac{x - x^k}{x^j - x^k}, \tag{19}$$

where x^j and x^k are nodal coordinates. The polynomials have the property that $\psi_j(x^i) = \delta_{ij}$, where δ_{ij} is the Kronecker delta and x^i is the nodal location. An $m-1$ order polynomial basis function is represented by m nodes.

The finite element method proceeds by multiplying the governing equation, Eq. (16), by test functions and integrating over each element volume

$$\int_\Omega d\mathbf{x} v_i \frac{\partial \mathbf{Q}^f}{\partial t} + \int_\Omega d\mathbf{x} v_i \frac{\partial \mathcal{F}}{\partial \mathbf{Q}^f} \cdot \frac{\partial \mathbf{Q}^f}{\partial \mathbf{x}} = \int_\Omega d\mathbf{x} v_i \mathbf{S}^f . \tag{20}$$

This integral equation is the weak form of the governing equation. The Galerkin method chooses the test functions to be the same as the basis functions, $v_i = \psi_i$, so the weak form of the governing equation with the solution expansion becomes

$$\int_\Omega d\mathbf{x} \psi_i \frac{\partial}{\partial t} \left(\sum_{j=1}^m \mathbf{q}_j \psi_j \right) + \int_\Omega d\mathbf{x} \psi_i \frac{\partial \mathcal{F}}{\partial \mathbf{Q}^f} \cdot \frac{\partial}{\partial \mathbf{x}} \left(\sum_{j=0}^m \mathbf{q}_j \psi_j \right) = \int_\Omega d\mathbf{x} \psi_i \mathbf{S}^f , \tag{21}$$

which is the element equation. Since the nodal values $\mathbf{q}_j$ are independent of x, the element equation can be rewritten as

$$\sum_{j=1}^m \left[\int_\Omega d\mathbf{x} \psi_i \psi_j \right] \frac{\partial \mathbf{q}_j}{\partial t} + \sum_{j=1}^m \left[\int_\Omega d\mathbf{x} \psi_i \frac{\partial \mathcal{F}}{\partial \mathbf{Q}^f} \cdot \frac{\partial \psi_j}{\partial \mathbf{x}} \right] \mathbf{q}_j = \int_\Omega d\mathbf{x} \psi_i \mathbf{S}^f . \tag{22}$$

The first integral is the element mass matrix for element e,

$$\mathcal{M}^e_{ij} = \int_\Omega d\mathbf{x} \psi_i \psi_j . \tag{23}$$

The element equation is integrated from time t to $t + \Delta t$, i.e. time level n to $n+1$, to give

$$\sum_{j=1}^m \mathcal{M}^e_{ij} \int_t^{t+\Delta t} dt \frac{\partial \mathbf{q}_j}{\partial t} = \sum_{j=1}^m \mathcal{M}^e_{ij} \left(\mathbf{q}_j^{n+1} - \mathbf{q}_j^n \right) . \tag{24}$$

Moving the spatially dependent terms of Eq. (22) to the right-hand side of the equation, integrating over Δt, and combining with the previous result yields

$$\sum_{j=1}^m \mathcal{M}^e_{ij} \frac{\mathbf{q}_j^{n+1} - \mathbf{q}_j^n}{\Delta t} = -\sum_{j=1}^m \left[\int_\Omega d\mathbf{x} \psi_i \frac{\partial \mathcal{F}}{\partial \mathbf{Q}^f} \cdot \frac{\partial \psi_j}{\partial \mathbf{x}} \right] \mathbf{q}_j + \int_\Omega d\mathbf{x} \psi_i \mathbf{S}^f , \tag{25}$$

where the right-hand side is computed using values appropriately averaged over the time interval $[t, t+\Delta t]$.

The CG method as described by Eq. (25) introduces no dissipation, and in regions of sharp gradients high frequency oscillations (Gibbs phenomenon) can develop. These oscillations indicate numerical dispersion and can be dampened by adding an artificial dissipation. This is achieved by introducing a term to Eq. (14) that consists of a second derivative of the conserved variables,

$$\frac{\partial \mathbf{Q}^f}{\partial t} + \nabla \cdot \mathcal{F} = \mathbf{S}^f + \nabla \cdot \left(\kappa \nabla \mathbf{Q}^* \right) , \tag{26}$$

where κ is the artificial diffusivity coefficient and is chosen to minimize the impact on the physical solution while minimizing numerical dispersion. The vector $\mathbf{Q}^*$ indicates that the variables being dissipated may be a subset of $\mathbf{Q}^f$.

Multiplying the dissipation term by the test functions, integrating over the element volume, and expanding $\mathbf{Q}^*$ with basis functions yields

$$\int_\Omega d\mathbf{x} \psi_i \frac{\partial}{\partial \mathbf{x}} \cdot \kappa \frac{\partial \mathbf{Q}^*}{\partial \mathbf{x}} = -\sum_{j=1}^m \left[\int_\Omega d\mathbf{x} \kappa \frac{\partial \psi_i}{\partial \mathbf{x}} \cdot \frac{\partial \psi_j}{\partial \mathbf{x}} \right] \mathbf{q}_j^* + \sum_{j=1}^m \left[\oint_{\partial\Omega} \mathbf{A} \cdot \frac{\partial \psi_j}{\partial \mathbf{x}} \kappa \psi_i \right] \mathbf{q}_j^* , \tag{27}$$

where the last term accounts for boundary conditions and is assumed to be equal across element boundaries since the solution for the electron species and the electromagnetic fields has C^0 continuity. Enforcing C^0 continuity is simplified by using the nodal representation given by Eq. (18) and placing nodes at the element boundaries. Nodes from neighboring elements overlap and the values at the overlapping nodes are set equal.

The CG method applied to the electron fluid and the electromagnetic fields of the two-fluid plasma model can be expressed in a simpler form by defining the element dissipation matrix

$$\mathcal{D}_{ij}^{e} = -\int_{\Omega} d\mathbf{x}\kappa \frac{\partial \psi_i}{\partial \mathbf{x}} \cdot \frac{\partial \psi_j}{\partial \mathbf{x}}, \tag{28}$$

and the element source vector

$$\mathbf{f}_{i}^{e} = \int_{\Omega} d\mathbf{x}\psi_i \mathbf{S}^{f}. \tag{29}$$

The element evolution equation can be written as

$$\mathcal{M}_{ij}^{e}\frac{\mathbf{q}_j^{n+1}-\mathbf{q}_j^{n}}{\Delta t} = -\left[\int_{\Omega} d\mathbf{x}\psi_i \frac{\partial \mathcal{F}}{\partial \mathbf{Q}^{f}} \cdot \frac{\partial \psi_j}{\partial \mathbf{x}}\right]\mathbf{q}_j + \mathbf{f}_i^{e} + \mathcal{D}_{ij}^{e}\mathbf{q}_j^{*} + \left[\oint_{\partial\Omega} \mathbf{A} \cdot \frac{\partial \psi_j}{\partial \mathbf{x}}\kappa\psi_i\right]\mathbf{q}_j^{*}, \tag{30}$$

where the summation over index j is assumed. Let $\mathbf{R}^{e}(\overline{\mathbf{q}_j})$ be the right-hand side of Eq. (30). $\mathbf{R}^{e}(\overline{\mathbf{q}_j})$ is computed using solution values that approximate the appropriately averaged values over the time interval $[t, t+\Delta t]$. Nodal values $\mathbf{q}_j^{n+1}$ are solved simultaneously for all elements. The element equations are assembled into a global system with global mass $\mathcal{M}$ and dissipation $\mathcal{D}$ matrices. The integral terms and the source vector $\mathbf{f}_i$ in Eq. (30) are evaluated by Gauss–Legendre quadrature rules and are also assembled into a global vectors. The correspondence between the element and global matrices is expressed through a connectivity matrix whose coefficient b_{ij} is the global node number corresponding to node j of element i. The element matrix coefficients $\mathcal{M}_{kl}^{e}$ are combined to give the global matrix according to

$$\mathcal{M}_{mn} = \sum_{e=1}^{E}\sum_{k=1}^{N}\sum_{l=1}^{N}\mathcal{M}_{kl}^{e}, \tag{31}$$

where global node numbers are defined using the connectivity matrix, $m = b_{ek}$, $n = b_{el}$. The mass matrix and dissipation matrices are assembled independently of each other. The total number of elements is E and the number of nodes per element is N. The resulting global matrix equation

$$\mathcal{M}\frac{\mathbf{q}^{n+1}-\mathbf{q}^{n}}{\Delta t} = \mathbf{R}(\overline{\mathbf{q}}) \tag{32}$$

can be solved to yield the solution for the electron fluid and electromagnetic field at the time level $n+1$.

Time integration for the CG method requires a matrix inversion to solve the global matrix equation even if the RHS is explicitly defined as $\mathbf{R}(\mathbf{q}_j^{n})$, while an implicit formulation only slightly complicates the solution method. However, an implicit solution method permits time steps larger than the short timescales dictated by the fast response of the electron fluid and electromagnetic field. Avoiding this limitation is a primary motivation for the BFEM and the physics-based decomposition.

The implicit formulation of the BFEM uses the θ-method [46] to solve the global evolution equation, which is written as

$$\mathcal{M}\frac{\mathbf{q}^{n+1}-\mathbf{q}^{n}}{\Delta t} = (1-\theta)\mathbf{R}(\mathbf{q}^{n}) + \theta\mathbf{R}(\mathbf{q}^{n+1}). \tag{33}$$

Choosing $\theta = 1$ gives the implicit backward Euler method, and $\theta = 0$ gives the explicit forward Euler method. Setting $\theta = 1/2$ gives the Crank–Nicolson method [47]. Because of its higher temporal accuracy, $\theta = 1/2$ is chosen for the BFEM implementation.

A Newton–Raphson method [48] is used to solve for $\mathbf{q}^{n+1}$. The Newton method yields an iterative process to find successively better approximations to the roots of a real-valued residual function, which for Eq. (33) is given by

$$\mathbf{G}(\mathbf{q}^{n+1}) = \frac{\mathcal{M}}{\Delta t}(\mathbf{q}^{n+1}-\mathbf{q}^{n}) - (1-\theta)\mathbf{R}(\mathbf{q}^{n}) - \theta\mathbf{R}(\mathbf{q}^{n+1}). \tag{34}$$

The Jacobian is

$$\mathcal{J}(\mathbf{q}^{n+1}) = \frac{\partial \mathbf{G}(\mathbf{q}^{n+1})}{\partial \mathbf{q}^{n+1}} = \frac{\mathcal{M}}{\Delta t} - \theta\frac{\partial \mathbf{R}(\mathbf{q}^{n+1})}{\partial \mathbf{q}^{n+1}}. \tag{35}$$

The Newton method is formulated as

$$\mathcal{J}(\mathbf{q}^{m})\Delta\mathbf{q} = -\mathbf{G}(\mathbf{q}^{m}), \tag{36}$$

where $\Delta\mathbf{q} = \mathbf{q}^m - \mathbf{q}^n$ and m is an iteration index. When the iteration equation, Eq. (36), converges, the solution at the next time level is given by

$$\mathbf{q}^{n+1} = \mathbf{q}^n + \Delta\mathbf{q}, \tag{37}$$

using the value from the previous time level and the solution for $\Delta\mathbf{q}$ from the Newton method.

3.2. Discontinuous Galerkin finite element method

Similar to the CG method, the DG method discretizes the computational domain into elements and expands the solution in a series of polynomial basis functions. However, the DG method does not enforce continuity of the solution across element boundaries. Unique solutions to the weak form of the governing equations are determined within each element by specifying element boundary fluxes that are defined in a consistent manner – the flux leaving an element equals the flux entering the adjacent element, e.g. Ref. [11]. The DG method that is incorporated into the BFEM is similar to the implementations of Refs. [49,35,50].

The DG method evolves the ion and neutral fluids of the multi-fluid plasma model. The governing equations are expressed by Eq. (14) where the vector of conserved variables excludes the electron fluid and electromagnetic fields. Namely,

$$\mathbf{Q}^s = [\mathbf{Q}_{i1}, \mathbf{Q}_{i2}, \ldots, \mathbf{Q}_{n1}, \mathbf{Q}_{n2}, \ldots],$$

where multiple ion and neutral species are possible. This subset of the governing equations accounts for the slower dynamics. The vector of conserved variables is expanded within each element using polynomial functions as

$$\mathbf{Q}^s(t,x) = \sum_{j=1}^{m} \mathbf{q}_j(t)\phi_j(x), \tag{38}$$

where ϕ_j are the spatial basis functions and $\mathbf{q}_j$ are the temporal coefficients. The s superscript, denoting slow dynamics, is omitted from the temporal coefficients to simplify the notation. The DG method uses a modal representation of the solution within an element, unlike the nodal representation of the CG method; therefore, the temporal coefficients in Eq. (38) do not directly represent values of the solution vector $\mathbf{Q}^s$. A modal representation simplifies the application of flux limiters [49,50]. Legendre polynomials of order $m-1$ are used as basis functions because they form an orthogonal basis,

$$\int_0^1 dx\phi_i\phi_j = \frac{1}{2j+1}\delta_{ij}, \tag{39}$$

which can be normalized to the element volume.

The governing equations of Eq. (14) that evolve $\mathbf{Q}^s$ are multiplied by the test functions, which are the same as the basis functions, and integrated over each element volume,

$$\int_\Omega d\mathbf{x}\phi_i \frac{\partial \mathbf{Q}^s}{\partial t} + \int_\Omega d\mathbf{x}\phi_i \nabla\cdot\mathcal{F} = \int_\Omega d\mathbf{x}\phi_i \mathbf{S}^s. \tag{40}$$

Integration by parts is applied to the second term and the above equation becomes

$$\int_\Omega d\mathbf{x}\phi_i \frac{\partial \mathbf{Q}^s}{\partial t} + \oint_{\partial\Omega} d\mathbf{A}\cdot\mathcal{F}\phi_i - \int_\Omega d\mathbf{x}\nabla\phi_i\cdot\mathcal{F} = \int_\Omega d\mathbf{x}\phi_i\mathbf{S}^s. \tag{41}$$

When the solution vector is expanded using Eq. (38) and the orthogonality of the basis functions are taken into account the first term of Eq. (41) simplifies to

$$\int_\Omega d\mathbf{x}\phi_i \frac{\partial \mathbf{Q}^s}{\partial t} = \sum_{j=1}^{m} \frac{\partial \mathbf{q}_j}{\partial t}\int_\Omega d\mathbf{x}\phi_i\phi_j = \frac{\partial \mathbf{q}_i}{\partial t}\frac{V^\Omega}{2i+1}, \tag{42}$$

where V^Ω is the volume of the finite element. The surface integral in Eq. (41) accounts for the fluxes across element boundaries, which are computed using a numerical flux, such as an approximate Riemann flux [1,51] or a Lax–Friedrichs flux [52]. The surface integral is evaluated using Gauss–Legendre quadrature over the element's surface. Simpler Lax–Friedrichs fluxes are typically adequate and are given at any point along the surface by

$$\mathcal{F} = \frac{1}{2}\left[\mathcal{F}(\mathbf{Q}_e^+) - \mathcal{F}(\mathbf{Q}_{e+1}^-)\right] - \frac{1}{2}|\lambda|(\mathbf{Q}_e^+ - \mathbf{Q}_{e+1}^-), \tag{43}$$

where $|\lambda|$ is the maximum characteristic speed (eigenvalue of the flux Jacobian) using surface values averaged from elements e and $e+1$, and superscripts $+$ and $-$ represent the values at the upper and lower boundaries of the elements. The volume integrals in Eq. (41) are also evaluated using Gauss–Legendre quadrature rules.

Using the relation given by Eq. (42) and rearranging the temporally and spatially dependent terms, Eq. (41) can be written as

$$\frac{\partial \mathbf{q}_i}{\partial t} = \frac{2i+1}{V^{\Omega}} \left(\int_{\Omega} d\mathbf{x} \phi_i \mathbf{S}^s - \oint_{\partial\Omega} d\mathbf{A} \cdot \mathcal{F}\phi_i + \int_{\Omega} d\mathbf{x} \nabla\phi_i \cdot \mathcal{F} \right) \equiv \mathbf{L}_i(\mathbf{Q}^s), \tag{44}$$

where $\mathbf{L}_i(\mathbf{Q}^s)$ is an operator containing all the spatially dependent term. An attractive feature of the DG method is the data locality of the spatial operator, which has a spatial dependency that is limited to nearest neighbor elements. The equation $\partial \mathbf{q}_i / \partial t = \mathbf{L}_i(\mathbf{Q}^s)$ can be integrated in time to advance the solution from time level n to $n+1$.

The time integration for the DG method uses the second order total variation bounded (TVB) Runge–Kutta time integration scheme [11], which is given as

$$\mathbf{q}_i^* = \mathbf{q}_i^n + \Delta t \mathbf{L}_i(\mathbf{Q}^{sn}) \tag{45}$$

$$\mathbf{q}_i^{n+1} = \frac{1}{2}\mathbf{q}_i^* + \frac{1}{2}\mathbf{q}_i^n + \frac{1}{2}\Delta t \mathbf{L}_i(\mathbf{Q}^{s*}), \tag{46}$$

where $\mathbf{Q}^{s*}$ is evaluated by Eq. (38) using the temporal coefficients $\mathbf{q}_i^*$.

The CFL stability condition of the DG method limits the CFL number as

$$\frac{\lambda_{max}^s \Delta t}{\Delta x} \leq \frac{1}{2p-1}, \tag{47}$$

where Δx is the size of the element, p is the order of the basis function, and λ_{max}^s is the largest characteristic speed. The system of equations being solved by the explicit RKDG method only includes the slower responding ion and neutral species and excludes the fast dynamics of the electron fluid and electromagnetic field. Therefore, the fastest characteristic speed for this subset of the governing equations is an ion or neutral acoustic speed and is typically much slower than the fastest characteristic speed for the complete system discussed in Sec. 2. With the explicit treatment of the ions and neutrals, the maximum time step size that satisfies Eq. (47) can be significantly larger than the time step size for an explicit treatment of the full multi-fluid plasma model.

3.3. Source treatment for the continuous and discontinuous Galerkin methods

The fluids and fields couple through the source terms of the governing equations. Source terms couple the solution variables $\mathbf{Q}^f$ that represent the fast dynamics of the system to the solution variables $\mathbf{Q}^s$ that represent the slow dynamics of the system. Therefore, the CG and DG methods must provide an accurate source treatment that is consistent between the two methods. Although the CG method uses a nodal representation and the DG uses a modal representation, converting the variables between the representations to compute the source terms is unnecessary.

Both the CG and DG methods solve weak formulations of the governing equations, so the source terms appear as integrals over the element volume in Eqs. (29) and (41). The source term integrals are computed numerically using quadrature rules, which require evaluating the integrand and hence the solution vector at specified spatial locations. The solution expansions given by Eqs. (18) and (38) allow the evaluation of $\mathbf{Q}^f$ and $\mathbf{Q}^s$ at any spatial position within an element. The source term integrands are thereby evaluated at the quadrature locations using the nodal and modal representations directly to compute the integrals.

4. Benchmarks and performance of the BFEM

The BFEM is applied to a set of problems with known analytic solutions. Spatial and temporal convergence tests are first performed to verify that the order of accuracy of the solution is in agreement with analytical results. The BFEM is benchmarked against the one-dimensional two-fluid plasma soliton problem [53] and the two-fluid electromagnetic shock tube problem [1,50]. These tests compare the computational time and accuracy of the BFEM with that of conventional finite volume and pure DG methods. The tests also evaluate the effects of the artificial dissipation in the CG portion of the method, and investigate the consequences of the implicit time integration on the solution. In addition, a three-fluid species separation problem is solved, which demonstrates the computational savings potential of the BFEM in a realistic application.

4.1. Linear advection: convergence study

The linear advection equation is a simple homogeneous hyperbolic equation that provides a test case to study the spatial and temporal convergence of the solution as the polynomial order for the solution is increased [35]. The DG and

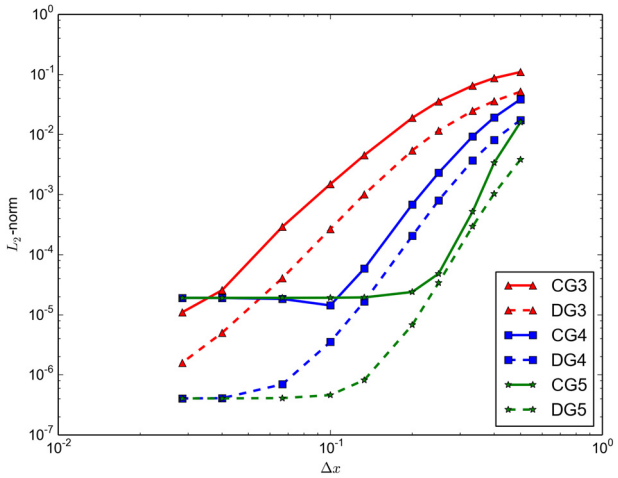

Fig. 1. Log–log plot of the L_2-norm of the error as a function of element size, Δx, for the linear advection problem using a fixed time step of $\Delta t = 1/800$ and spatial orders 3, 4, and 5 for the CG and the DG methods. The artificial dissipation coefficient used with the CG method is $\kappa = 10^{-7}$. The linear portion of each line has a slope that corresponds to the order of accuracy of the numerical method. Both methods converge as expected. Higher order CG methods saturate at larger values of Δx because the dissipation is applied at each node, and higher order methods have more nodes and therefore more dissipation.

CG components of the BFEM are separately used to solve the linear advection equation. The accuracy of the solution is determined by the order of accuracy of the numerical method. The one-dimensional linear advection equation is given by

$$\frac{\partial Q}{\partial t} + \frac{\partial Q}{\partial x} = 0, \tag{48}$$

where Q is a scalar variable and the advection speed is set to one. A Gaussian pulse is initialized with $Q(x) = e^{-10(x-2)^2}$ on a domain $[0, 10]$. The pulse's peak starts at $x = 2$ and propagates $x = 8$ over a total time interval of $t \in [0, 6]$ and is compared to the analytical solution given as $\hat{Q}(x) = e^{-10(x-8)^2}$. The error in the numerical solution is calculated by evaluating the L_2-norm as

$$||\Delta Q||_2 = \sqrt{\frac{1}{n}\sum_{i=1}^{n}\left(\hat{Q}(x_i) - Q(x_i)\right)^2}. \tag{49}$$

where $\hat{Q}$ is the analytical solution and Q is the numerical solution. The positions x_i represents the quadrature locations for both the DG and CG methods, and n is the total number of quadrature points [35].

Fig. 1 shows the L_2-norm of the error for the advected pulse using a fixed $\Delta t = 1/800$ with different order polynomial spatial basis functions for the DG and the CG methods. Using a fixed time step size isolates the spatial convergence. The plot shows that for basis functions of the same order the CG and DG methods converge at the same rate as the grid is refined. The slope of the curves for similar order DG and CG should be the same even though the DG method is slightly more accurate than then CG one. The L_2-norm of the CG method plateaus around 10^{-5} due to the artificial numerical dissipation, which damps the solution and decreases the peak of the original Gaussian shape. The required value of κ for stability decreases as the polynomial order is increased. The fixed value of $\kappa = 10^{-7}$ is the minimum value required for the coarsest grid for spatial order three and used for all simulations for consistency, allowing only on variable to change.

To test the temporal convergence rate, a fixed time step size is chosen. The time step size is set as $\Delta t = \Delta x$ for all polynomial orders of the spatial basis functions, which isolates the temporal convergence. For the CG method, a value of $\theta = 0.5$ is selected to give the second-order accurate Crank–Nicolson method. The DG method uses a second-order TVB Runge–Kutta time integration. Fig. 2 shows the calculated L_2-norm for the advection problem using a fixed CFL number. The slope of the lines for both methods is two for all polynomial orders of the spatial basis functions. The convergence rates of the error for a fixed CFL verify that the temporal integration is second-order accurate for the implicit CG method as well as the explicit DG method.

4.2. Plasma soliton: accuracy and computational cost

The propagation of a one-dimensional plasma soliton [53] is modeled using the multi-fluid plasma model. This problem is used to study the accuracy and computational cost of the BFEM as compared with an explicit DG method. The soli-

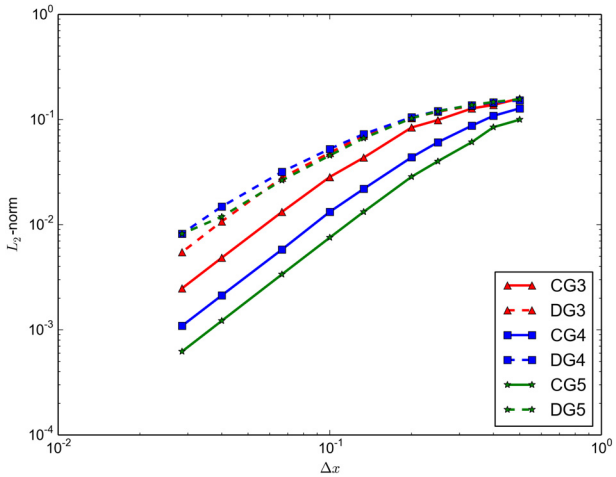

Fig. 2. Log–log plot of the L_2-norm of the error as a function of element size, Δx, for the linear advection problem using a fixed CFL of one and spatial orders 3, 4, and 5 for the CG and the DG methods. The artificial diffusivity coefficient used with the CG method is $\kappa = 10^{-7}$. The linear portions of all lines have a slope of two corresponding to the temporal order of accuracy of both the implicit CG and explicit DG portions of the BFEM method.

Table 1
Total computational time and time savings for plasma soliton simulations using the BFEM as compared to an explicit DG method for different values of electron to ion mass ratio and of the ratio of the speed of light to the ion sound speed.

Case	m_i/m_e	c/c_{si}	DG time (s)	BFEM time (s)	BFEM cost over DG
1	25	$10/\sqrt{2}$	0.32	37.7	+11681%
2	100	$10/\sqrt{2}$	1.28	37.7	+2845%
3	500	$10/\sqrt{2}$	6.82	37.7	+452.8%
4	1000	$10/\sqrt{2}$	12.4	38.2	+208.1%
5	1836	$10/\sqrt{2}$	23.5	40.4	+71.91%
6	3672	$10/\sqrt{2}$	47.2	39.2	−16.95%
7	3672	$100/\sqrt{2}$	520	265	−49.04%
8	3672	$1000/\sqrt{2}$	5274	2735	−48.14%

ton consists of a two-fluid plasma composed of an electron fluid and an ion fluid, and offers a simple test case for the BFEM. The expected solution is smooth, which requires minimal artificial dissipation for achieving stable solutions with the BFEM, eliminating the detrimental effect on convergence that is described in the previous section. The artificial diffusivity coefficient κ, used in Eq. (26), is set to a value of 10^{-10}.

The normalized variables of the two-fluid plasma model are initialized with a uniform transverse magnetic field $B_z = 1.0$, uniform ion and electron temperatures $T_i = T_e = 0.01$, no fluid velocity $\mathbf{u}_i = \mathbf{u}_e = \mathbf{0}$, and unitary charges $q_i = -q_e = 1$. The initial particle number densities produce a Gaussian pulse on top of a background value $n_i = n_e = 1 + e^{-10(x-6)^2}$ on a domain $x \in [0, 12]$. The ratio of specific heats as used in Eq. (5) is set to $\Gamma = 2$. The simulation uses 512 second-order elements both for the BFEM and for the comparison case using the DG method. Periodic boundary conditions are used.

It is common practice in plasma simulations to artificially decrease the ion to electron mass ratio as well as the ratio of speed of light to ion sound speed [54]. This is done to relax the numerical time step restriction imposed by electron plasma frequency and the speed of light. Using an artificial mass ratio and/or an artificial speed of light can, however, affect the physics of the problem. To evaluate the effect of using physical and unphysical parameters, the computational cost of the BFEM versus the DG method is compared for artificial and realistic mass and speed ratios.

Since the implicit CG component of the BFEM allows time steps that are unconstrained by the electromagnetic fields or electron fluid, computational savings of the BFEM over the explicit DG method are achieved when using physical values for the ion to electron mass ratio and the speed of light to ion sound speed ratio. Table 1 shows the computational time needed to advance the solution from normalized time $t = 0$ to $t = \sqrt{2}/120 L/c_{si}$ for different mass ratios and normalized speeds of light. The ion sound speed is defined as $c_{si} = \sqrt{\Gamma p_i/\rho_i}$. For a mass ratio of 25, the DG method is considerably faster than the BFEM; however, as the mass ratio is increased by decreasing the electron mass, the computational time of the DG method increases while that of the BFEM remains about the same. This is due to the fact that the decreasing electron mass increases the electron plasma frequency, which needs to be resolved when explicit time integration is used. The speed of light to ion sound speed ratio has a bigger impact on the computational time than the mass ratio. The explicit DG method requires that the time step size be decreased as the speed of light increases to satisfy the CFL stability condition given by

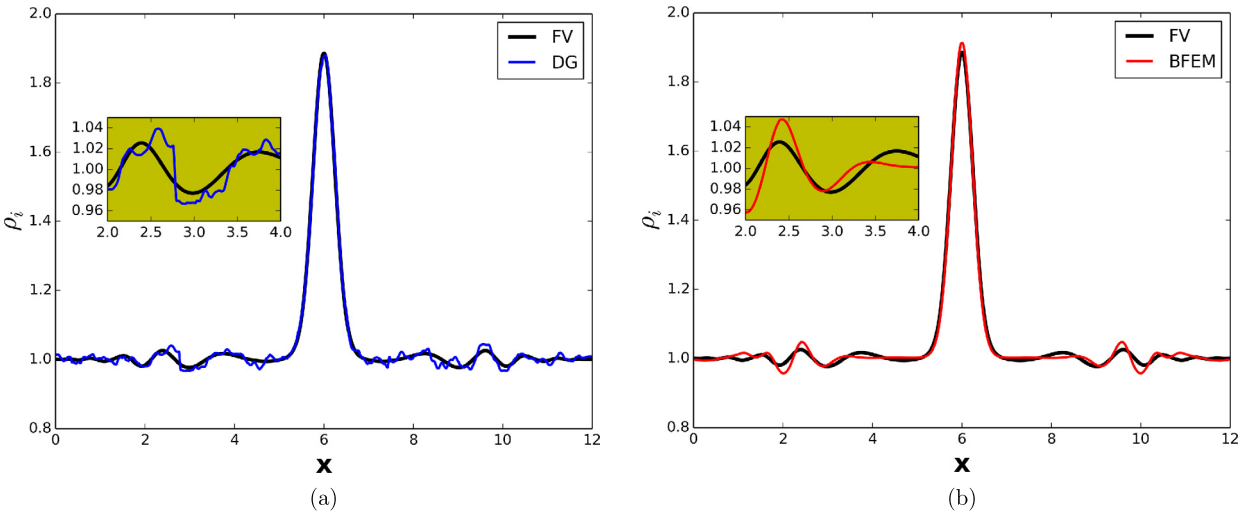

Fig. 3. Ion density profiles for the plasma soliton problem at $t = \sqrt{2}/30 L/c_{si}$ are shown for the explicit DG solution and the BFEM solution using 512 second-order elements. The simulations use a realistic mass ratio and normalized speed of light. The solutions are compared to a converged FV solution of 5000 cells. Ion density fluctuations propagate from the center of the domain towards the boundaries. Both methods resolve the oscillations of the problem, but the BFEM exhibits phase error since it does not resolve the electron plasma frequency. Second-order BFEM is used.

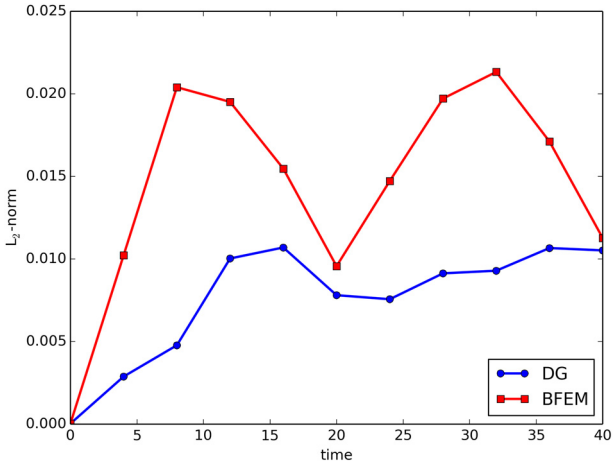

Fig. 4. L_2-norm of the relative error, see Eq. (50), in the ion density solutions for the plasma soliton problem from the DG method and the BFEM as a function of time. Realistic values for the ion to electron mass ratio and the speed of light to ion sound speed ratio are used. The DG method produces a more accurate solution than the BFEM. The BFEM error relative to the converged solution – as measured by the L_2-norm – is only about 1.5%, this corresponds to case 8 from Table 1.

Eq. (47). Therefore, as the ratio of speed of light to ion sound speed approaches realistic values, the BFEM computational time becomes considerably less than that of the DG method.

The ion density solutions at $t = \sqrt{2}/30 L/c_{si}$ from the DG method and the BFEM using 512 second-order elements are shown in Fig. 3 and compared to a converged solution with 5000 cells using a finite-volume high-resolution wave propagation method [18]. In this case the plasma soliton is initialized with $m_i/m_e = 1836$ and $c/c_{si} = 1000/\sqrt{2}$. The DG solution exhibits a large amount of dispersion, which appears when a realistic mass ratio is used. The reason for the dispersion on the DG method is not well understood at this point, further studies are need. The BFEM has a higher peak value than the other methods because both the DG method and the FV method can be more dissipative even for smooth solutions. This is due to the fact that both the FV and DG method use flux limiters that tend to decrease value on those cases. Fig. 3 also shows that the BFEM solution has phase errors due to the fact that the electron plasma frequency is not resolved. The phase error is evidenced by the BFEM solution being spatially shifted relative to the converged FV solution. Phase error is expected whenever high-frequency dynamics are not resolved by implicit time integrators. The dissipation in the BFEM method comes from the artificial dissipation term, Eq. (26), but for smooth solutions the value of κ can be small as in this case where $\kappa = 10^{-10}$.

Fig. 4 plots the evolution over time of the L_2-norm of the relative error for the DG method and the BFEM when using physical values for the ion to electron mass ratio and the speed of light to ion sound speed ratio. The relative error is

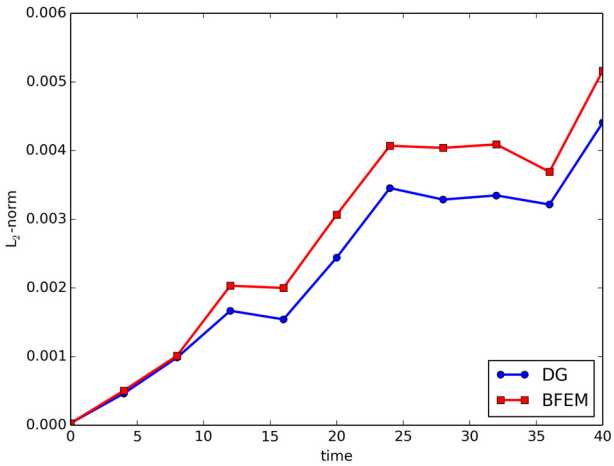

Fig. 5. L_2-norm of the relative error for the plasma soliton solution from the DG method and the BFEM as a function of time for a case where $m_i/m_e = 1$. The L_2-norms for the DG method and the BFEM are comparable since both methods use the same time step size and resolve the electron plasma frequency.

defined as

$$\frac{\rho_i^k - \rho_i^c}{\rho_i^c}, \tag{50}$$

where ρ_i^c is the mass density for the converged solution and ρ_i^k represents the solution given by the DG method or BFEM. The error is evaluated at each quadrature point (DG) or the nodal values (BFEM), and compared to the corresponding cell average (FV) at the same physical location. The L_2-norm of the DG error is lower than that of the BFEM error, and the BFEM error relative to the converged solution is approximately 1.5%. It is important to note that the BFEM resolution is only 10% of the converged solution resolution. The BFEM solution has a larger error because the DG and converged solutions are obtained using explicit time integration, which resolves the electron plasma frequency, whereas the BFEM does not resolve the electron plasma frequency. A fully explicit treatment is expected to be more accurate, but it is not always feasible or desired for stiff problems. The oscillatory behavior of the L_2-norm for the BFEM continues even for longer time intervals.

Fig. 5 compares the L_2-norm of the relative error for the DG method and the BFEM for a plasma soliton simulation in which the ion to electron mass ratio is one. The errors for the DG method and BFEM are comparable since the time step sizes are the same, and both methods resolve the electron and ion plasma frequencies.

The soliton problem demonstrates that the BFEM is less computationally costly than the DG method for problems where realistic ion to electron mass ratio and speed of light to ion sound speed ratio are used. In an hydrogen plasma, a realistic ion to electron mass ratio is 1836 (Table 1, case 5), which is at the lowest limit of mass ratios. For realistic fusion plasmas, the explicit time step limitation is even more restrictive because the ion to electron mass ratio is two or three times larger (see Table 1, case 8). Thus for fusion-relevant plasmas the BFEM offers considerable computational cost savings over the DG method, and it offers an even bigger advantage in plasma applications that use non-hydrogen plasmas where mass ratios would be even larger.

4.3. Electromagnetic plasma shock problem

The BFEM is applied to the two-fluid version of the electromagnetic plasma shock problem [55] as presented in Refs. [1, 35,50]. The electromagnetic plasma shock problem offers a comprehensive physics test for the BFEM because it exhibits the different limits of MHD behavior and of multi-fluid plasma effects by changing the ion Larmor radius, r_L. Note that MHD assumes the limit of $r_L \to 0$, and multi-fluid plasma model allows for arbitrary values of r_L.

The electromagnetic plasma shock is initialized with a discontinuity in the variables such that half of the domain is at one state and the other half is at another state. For the test case presented here, the mass ratio $m_i/m_e = 1836$. The problem is described in detail in Ref. [1]. The solution features are shown in Fig. 6 for the case with $r_L = 0.73$. From left to right the structures are: a fast rarefaction wave (FR), a slow compound wave (SC), a contact discontinuity (CD), a slow shock (SS), and another fast rarefaction wave (FR). For ion Larmor radii comparable to or smaller than the domain size, the ion fluid is tightly bound to the magnetic field and the solution contains wave-like structures. These structures are fast electromagnetic waves, which propagate faster than MHD waves and can be seen at the left of the first FR in Fig. 6. The fast waves, which include the whistler wave, correspond to the right-hand and left-hand circularly polarized plasma waves that propagate parallel to the magnetic field.

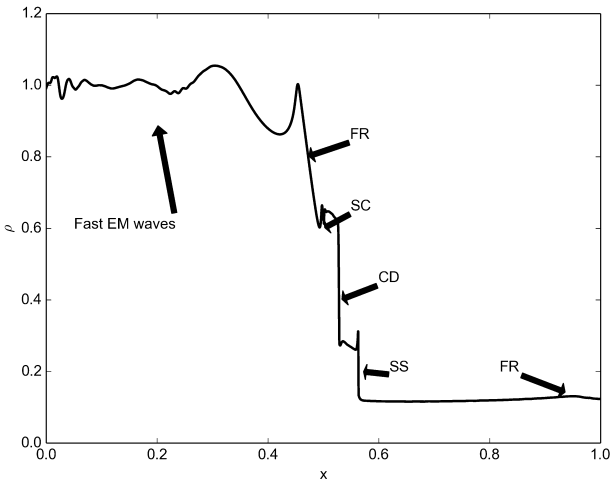

Fig. 6. The solution features of the electromagnetic plasma shock for $r_L = 0.73$ are a fast rarefaction wave (FR), a slow compound wave (SC), a contact discontinuity (CD), a slow shock (SS), and another fast rarefaction wave (FR). The solution also shows fast electromagnetic waves (including the whistler wave) that propagate faster than MHD waves [1].

The electromagnetic plasma shock is initialized by setting the two-fluid plasma variables to

$$\begin{bmatrix} n_e \\ u_e \\ v_e \\ w_e \\ p_e \\ n_i \\ u_i \\ v_i \\ w_i \\ p_i \\ B_x \\ B_y \\ B_z \\ E_x \\ E_y \\ E_z \end{bmatrix}_{\text{left}} = \begin{bmatrix} 1.0 \\ 0 \\ 0 \\ 0 \\ 0.5\times10^{-4} \\ 1.0 \\ 0 \\ 0 \\ 0 \\ 0.5\times10^{-4} \\ 0.75\times10^{-2} \\ 1.0\times10^{-2} \\ 0 \\ 0 \\ 0 \\ 0 \end{bmatrix}, \quad \text{and} \quad \begin{bmatrix} n_e \\ u_e \\ v_e \\ w_e \\ p_e \\ n_i \\ u_i \\ v_i \\ w_i \\ p_i \\ B_x \\ B_y \\ B_z \\ E_x \\ E_y \\ E_z \end{bmatrix}_{\text{right}} = \begin{bmatrix} 0.125 \\ 0 \\ 0 \\ 0 \\ 0.05\times10^{-4} \\ 0.125 \\ 0 \\ 0 \\ 0 \\ 0.05\times10^{-4} \\ 0.75\times10^{-2} \\ -1.0\times10^{-2} \\ 0 \\ 0 \\ 0 \\ 0 \end{bmatrix}, \tag{51}$$

for the left and right halves of the domain. The parameters used for the problem are obtained from Ref. [1], and are $c/c_{si} = 110$, $r_L = 0.73$, $\Gamma_e = \Gamma_i = \frac{5}{3}$ and the ion to electron mass ratio is $m_i/m_e = 1836$. A grid resolution of 512 second-order elements is used. Time is normalized to the ion cyclotron time $\tau_c = 1/\omega_{ci}$.

The solution from the BFEM is compared to a solution from the DG method [50] and to the finite-volume wave propagation method [18]. Fig. 7(a) shows the mass density profile at time $t = 0.05\tau_c$ for all three methods. The BFEM solution smooths the physical oscillations in the solution due to the artificial dissipation and is discussed in more detail in Sec. 4.3.2. The BFEM also does not resolve the fast electromagnetic waves, which are driven by electron dynamics. Fig. 7(b) shows B_y which is smooth and represented by the CG portion of the BFEM, showing that there is good agreement between all the methods where the electron dynamics is not very relevant.

4.3.1. Implicit and explicit time integration comparison

As evident in Eq. (47), the CFL condition depends on the characteristic speeds of the system, the species speeds of sound, $c_{s\alpha}$, and the speed of light, c. Moreover, the temporal discretization must also resolve the species cyclotron frequencies $\omega_{c\alpha} = q_\alpha B/m_\alpha$, and the species plasma frequencies $\omega_{p\alpha} = \sqrt{n_\alpha q_\alpha^2/\epsilon_0 m_\alpha}$, as described in Sec. 2. The initialization parameters for the electromagnetic plasma shocks studied are shown in Table 2.

The maximum explicit time step size is determined from these parameters by the following expression,

$$\Delta t_{max} = \min\left(\frac{\Delta x}{c_{se}}, \frac{\Delta x}{c_{si}}, \frac{\Delta x}{c}, \frac{\beta}{\omega_{ce}}, \frac{\beta}{\omega_{ci}}, \frac{\beta}{\omega_{pe}}, \frac{\beta}{\omega_{pi}}\right), \tag{52}$$

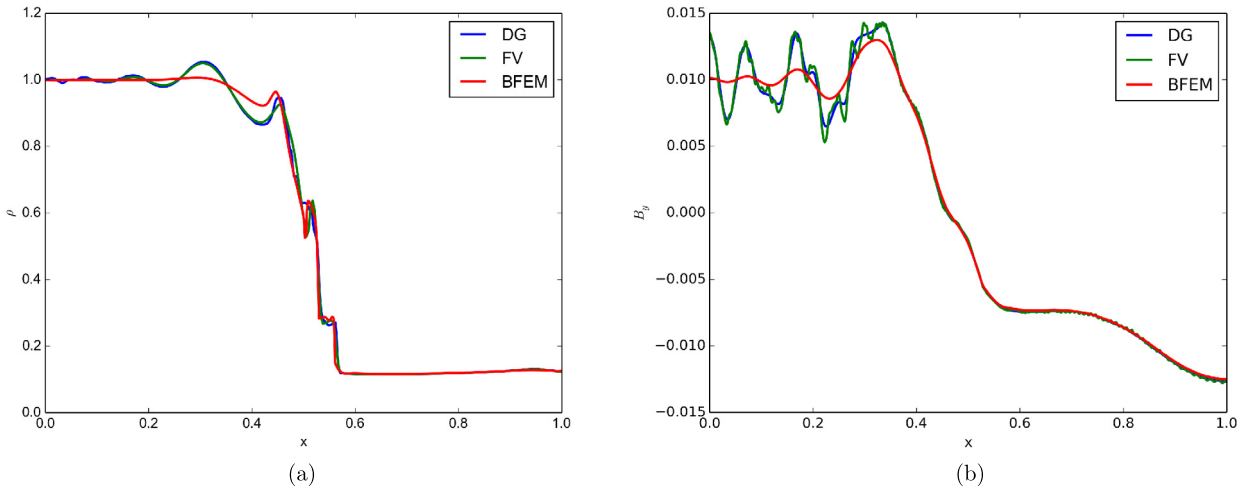

Fig. 7. The total mass density, $m_i n_i + m_e n_e$, and y-component of magnetic field are plotted for the electromagnetic plasma shock problem at $t = 0.05\tau_c$, when $c/c_{si} = 110$ and $m_i/m_e = 1836$. Second-order BFEM is used. The main features of the problem are captured by all three methods, but the BFEM does not properly resolve the fast electromagnetic waves, which require accurately resolving the electron dynamics by using a fully explicit treatment.

Table 2
Characteristic speeds and frequencies for the electromagnetic shock problem.

	Electron	Ion
c	1.0	1.0
$c_{s\alpha}$	3.9×10^{-1}	9.1×10^{-3}
$\omega_{c\alpha}$	1.8×10^{2}	1.0×10^{-1}
$\omega_{p\alpha}$	4.3×10^{2}	1.0×10^{1}

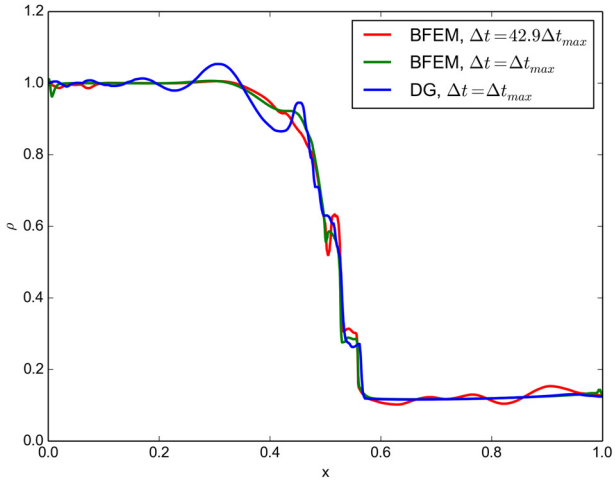

Fig. 8. The total mass density, $m_i n_i + m_e n_e$, is plotted for the electromagnetic plasma shock problem at $t = 0.05\tau_c$ using different time step size Δt. Second-order BFEM is used. The time step size is expressed relative to Δt_{max}, which corresponds to the maximum value allowed for explicit methods based on the CFL condition. Note that $\Delta t = 42.9\Delta t_{max}$ is the maximum time step allowed by the BFEM, where the ion dynamics restrict the time step size.

where β is the number of time points required to resolve an oscillation, typically, $\beta = 1/10$. The electron plasma frequency imposes the most stringent restriction on the time step size, $\Delta t_{max} = 2.33 \times 10^{-4}$. This restriction is particularly severe for methods that use fully explicit time integration. Since in the BFEM the electron fluid and the electromagnetic fields are advanced implicitly, the time step restrictions only depend on the slower ion and neutral fluids. Therefore, the BFEM permits larger time steps.

Fig. 8 compares the total mass density solution for BFEM using a time step equal to the explicit time step limit, $\Delta t = \Delta t_{max}$, with a solution using a larger implicit time step, $\Delta t = \sqrt{m_i/m_e}\Delta t_{max} = 42.9\Delta t_{max}$. The implicit time step is limited by the ion plasma frequency. The solution attained using the implicit Δt resolves all the main features of the problem

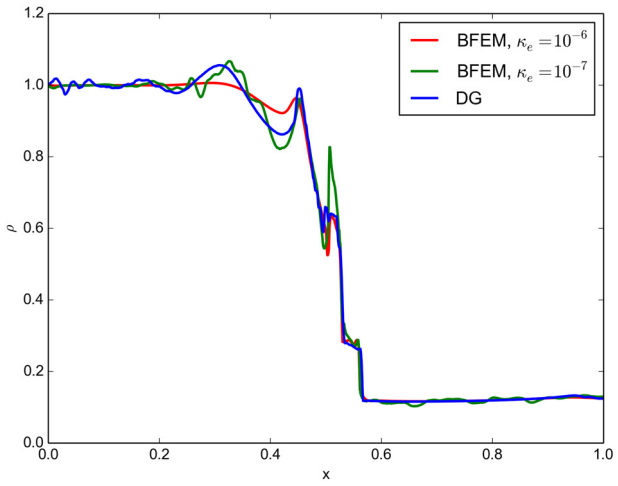

Fig. 9. The total mass density, $m_i n_i + m_e n_e$, is plotted for the electromagnetic plasma shock problem to demonstrate the effect of varying the artificial dissipation on the electron fluid, κ_e, for fixed electromagnetic artificial dissipation $\kappa_{EM} = 10^{-4}$. The solution for $\kappa_e = 10^{-7}$ captures the wave-like behavior of the electromagnetic plasma shock problem. The amplitude of the compound wave increases, and the right fast rarefaction wave is not visible. Second-order BFEM is used.

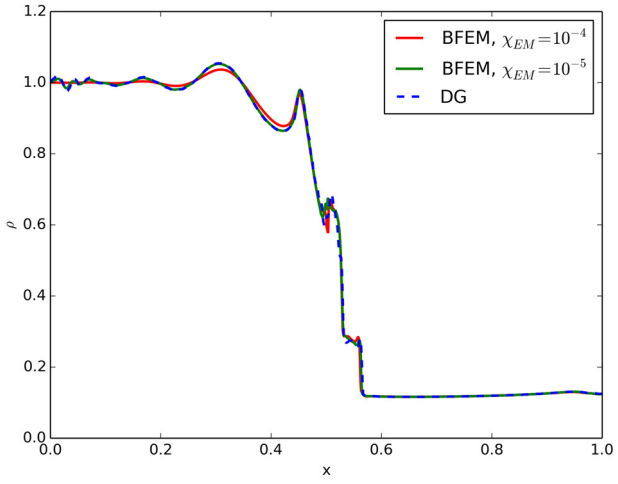

Fig. 10. The total mass density, $m_i n_i + m_e n_e$, is plotted for the electromagnetic plasma shock problem where the artificial dissipation on the electromagnetic fields is decreased from $\kappa_{EM} = 10^{-4}$ to 10^{-5}, and second-order BFEM is used. The electron fluid artificial dissipation is fixed at $\kappa_e = 10^{-6}$. The reduced dissipation solution agrees better with the solution from the DG method, reinforcing the point that the wave-like behavior arises from the interaction of the electron fluid with the electromagnetic fields. Second-order BFEM is used.

except the fast rarefaction wave, which should be ahead of the slow shock, but instead there are small oscillation ahead of the SS. The slow compound wave (SC) is better resolved with the larger time step of the BFEM because this wave is a feature of the ion dynamics.

4.3.2. Effects of artificial dissipation

As described in Sec. 3.1, an artificial dissipation term is added to the governing equations for the electron fluid and electromagnetic fields to damp numerical oscillations that are produced by the CG method in regions of sharp gradients in the solution. The artificial diffusivity coefficient κ scales the amount of artificial dissipation applied to the electron fluid and electromagnetic fields. If κ is too small the solution develops high amplitude node-to-node oscillations that grow over time, making the solution of the nonlinear Newton solver more stiff and requiring more iterations to converge [35]. On the other hand, if κ is too big the solution smooths relevant features of the solution producing an inaccurate result.

It is possible to apply different values of κ for the electron equations and electromagnetic field equations, e.g. κ_e and κ_{EM}. Reducing the artificial dissipation coefficient in the electron fluid (κ_e) from 10^{-6} to 10^{-7} while keeping κ_{EM} fixed makes the compound wave more distinct as shown in Fig. 9. The oscillations due to Langmuir and whistler waves are also more visible. However, the second fast rarefaction wave (right-most FR) is not resolved, and small oscillations are present instead. Decreasing the artificial dissipation applied to Maxwell's equations while keeping κ_e fixed allows the BFEM solution to better resolve the oscillations due to the fast electromagnetic waves. Fig. 10 shows the total mass density for

the electromagnetic plasma shock problem when the electron fluid dissipation is $\kappa_e = 10^{-6}$ and the electromagnetic field artificial dissipation is varied from $\kappa_{EM} = 10^{-4}$ to $\kappa_{EM} = 10^{-5}$. In addition, the fast rarefaction wave is better resolved with the smaller value of κ_{EM}.

Overall there is remarkable agreement between the BFEM solution and the computationally more expensive DG method solution. It is evident from the electromagnetic plasma shock results presented in Figs. 9 and 10 that artificial dissipation plays an important role in the accuracy of the BFEM solution. Thus the BFEM can be further improved by devising a systematic means of calculating the parameter κ or using a different form of artificial dissipation.

4.4. Species separation in fusion capsule implosions

The multi-fluid plasma model is applicable to problems where the plasma is composed of multiple species that exhibit dynamics at different scales. A motivating problem is the species separation [42] that can occur during the implosion phase of inertial confinement fusion (ICF) capsules, where deuterium and tritium are heated and compressed to fusion conditions. The compression process uses laser-driven shocks that produce electric fields [56], which can cause the deuterium to accelerate faster than the tritium. The phenomenon is not captured by single-fluid plasma models. Low neutron yield measurements [57] point to the possibility of fuel stratification caused by baro-diffusion [56] (pressure gradient-driven diffusion) that causes the separation of the ion species during the implosion.

The multi-fluid plasma for this problem is composed of two ion fluids, deuterium and tritium, and an electron fluid. The dynamics of the ions, electrons, and electromagnetic fields occur at a vastly different timescales, which introduces numerical stiffness making this problem ideally suited for the BFEM. The different timescales in the ICF fuel species separation problem result from the characteristic speeds and frequencies for the constituent species. The differences are particularly large when realistic speed of light and species masses are used.

Following the problem setup in Ref. [42], a Cartesian geometry is used and the plasma is initialized with a discontinuity in the parameters. The left half of the domain ($x < 0$) has a total ion density given by $\sum_\alpha n_\alpha = 4 \times 10^{19}$ cm^{-3}, where the sum is only over the ion species, with all species having a temperature of $T_\alpha = 100$ eV. The right half of the domain ($x \geq 0$) has a total ion density given by $\sum_\alpha n_\alpha = 1 \times 10^{19}$ cm^{-3} with all species having a temperature of $T_\alpha = 10$ eV. The plasma is initialized to be charge neutral everywhere, $n_e = \sum_\alpha Z_\alpha n_\alpha$, where the sum is again only over the ion species. Heat flux and viscous effects are neglected. The computational domain is $x \in [-30\ \mu\text{m}, 30\ \mu\text{m}]$, and zero normal gradient boundary condition are applied at the boundaries. The speed of light to proton sound speed ratio (c/c_{sp}) is 3065 and the proton to electron mass ratio is 1836. The ion species are characterized by ion mass ratio in relation to a proton mass, $\mu = m_\alpha/m_p$ and by the ionization state, $Z = q_\alpha/e$. The species separation from the deuterium is magnified by using a heavier second ion species with $\mu = 10$, instead of $\mu = 3$ corresponding to tritium.

Fig. 11 compares the ion number densities at $t = 150$ ps for simulations with an electron CFL number of 1 and an electron CFL number of 20. An electron CFL number of 1 restricts the time step size to resolve all electron characteristic timescales. The ion species separation is the same for both cases but the oscillations behind the shock front differ. This may be due to the fact that the electron dynamics are not fully resolved with an electron CFL number of 20. The effect of electron CFL number on the required computational time (defined as the total elapsed time) and solution accuracy is shown in Fig. 11(c). There it can be seen that there are considerable CPU cost saving as the CFL number is increased, although the gains are minimal after CFL = 10. The L_2-norm (Eq. (49)) increases after an electron CFL number of 10 but remains small.

5. Conclusion

A blended finite element method (BFEM) is presented for the multi-fluid plasma model. The method uses a DG spatial discretization combined with explicit Runge–Kutta time integration to describe the ion and neutral fluids and a CG spatial discretization combined with implicit Crank–Nicolson time integration for the electron fluid and electromagnetic fields. The DG method accurately captures shocks and discontinuities that can occur in the ion and neutral fluids, and the CG method efficiently and robustly computes smooth solutions for the electron fluid and electromagnetic fields. The physics-based decomposition of the algorithm into implicit CG and explicit DG portions yields numerical solutions that resolve the desired timescales and match the expected solution structure.

Each component of the numerical method is independently verified to converge at the expected order of accuracy. The two-fluid soliton problem is used to compare the computational cost of the BFEM to an explicit DG method. For unphysical values of the ion to electron mass ratio and speed of light to ion thermal speed ratio, the DG method is more computationally efficient than the BFEM. However, for realistic values of the mass ratio and normalized speed of light, the BFEM is less costly than the DG method. It is worth noting that for non-hydrogen plasmas, the mass ratio for the ion species relative to electrons can be many times greater than 1836, and even for fusion hydrogen plasmas the ion fluids are deuterium and tritium, so the mass ratio is 3672. In these cases the computational cost savings offered by the BFEM over the DG method are considerable.

The BFEM and DG method are further compared using the electromagnetic plasma shock problem. The total mass density from DG and BFEM solutions are compared to solutions given by a finite-volume high-resolution wave propagation method. The electron fluid and the electromagnetic field equations are advanced implicitly using a time step 42.9 times larger than the time step required for an explicit method. The fast electromagnetic waves and the fast rarefaction wave are not

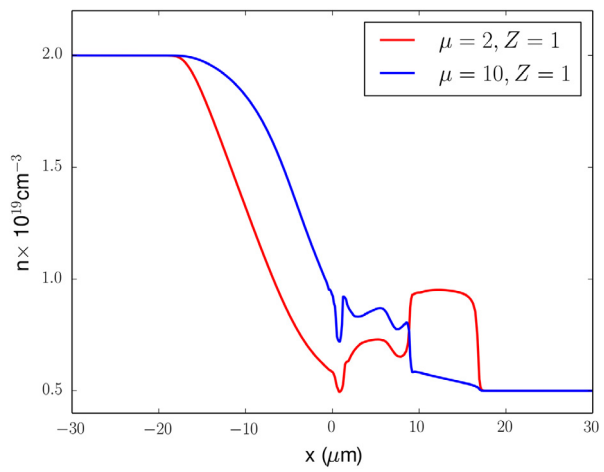

(a) Electron CFL=1

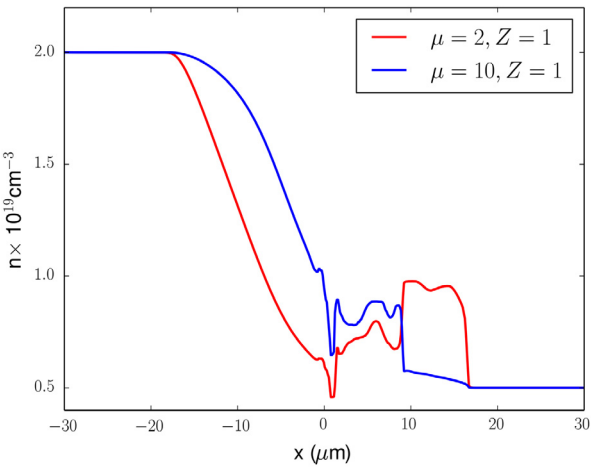

(b) Electron CFL=20

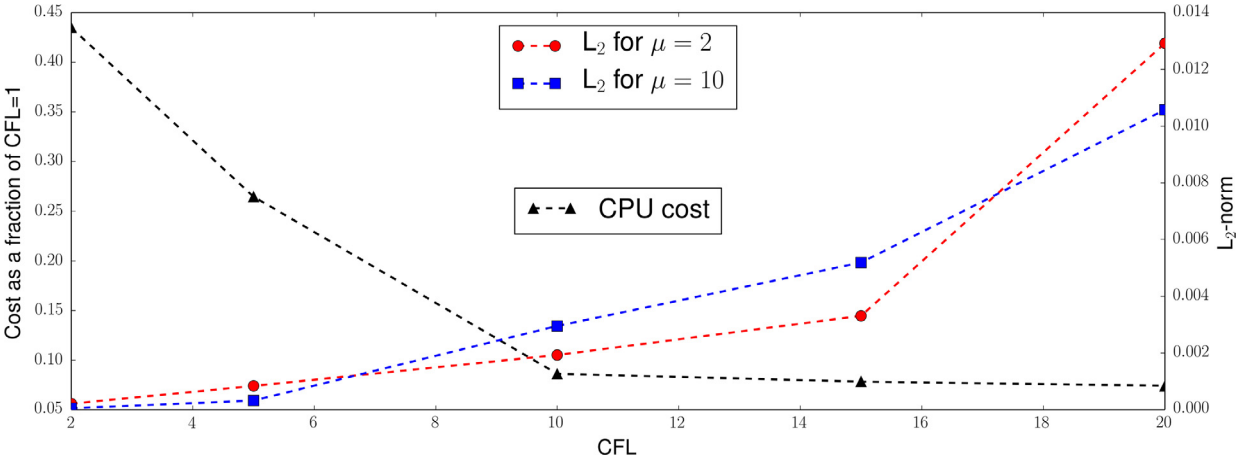

(c) Cost vs. Accuracy

Fig. 11. Depicted are the ion densities from a multi-fluid plasma simulation of the species separation problem composed of two ion fluids ($\mu = 2$ and $\mu = 10$) and an electron fluid using (a) an electron CFL number of 1, a time step size that resolves all electron characteristic timescales, and (b) an electron CFL number of 20. The ion species separation in both cases is the same although the solution behind the shock fronts differ. (c) The L_2-norm of the densities and the computational time for different electron CFL numbers are shown. The CPU time is calculated as a fraction of the computational time used for the case with electron CFL number of 1. The solution error increases as the computational time decreases.

resolved, but the location of the shock, contact discontinuity, and compound wave are accurately computed. The artificial dissipation added to the CG portion of the BFEM is adjusted for each equation system independently to produce more physically accurate results. When the artificial dissipation for Maxwell's equations is reduced by a factor of ten, there is remarkable agreement between the DG and BFEM results. This shows that artificial dissipation plays an important role in BFEM solutions.

Application of the BFEM to the multi-fluid plasma problem of species separation in ICF capsules demonstrates the ability of the method to take time step sizes that are much larger than the electron timescales. The method generates stable solutions that capture the overall ion structures but at a significantly lower computational cost.

The BFEM has large potential to be useful in problems where the slow dynamics are of primary interest, but the fast dynamics still play an important role, i.e. problems that span a multitude of temporal and spatial scales. The method offers a computationally efficient means of modeling plasma dynamics using realistic parameters. The BFEM can be further improved by dynamically adjusting the artificial dissipation. While the results presented are for one-dimensional applications, the extension to multiple dimensions is straightforward. The reduction in computational cost achieved by the BFEM is due to fast dynamics being treated implicitly. This means that the cost savings are expected to hold for higher dimensions. The DG method takes less computational time to advance the solution by one time step, however Δt is much smaller than that of the BFEM. Thereby a fully explicit DG solution takes many more time steps, independent of the dimensionality, which also means that the computational cost savings using the BFEM only occur for relatively large implicit time-steps compared to

explicit time-steps. The physics-informed blending of the CG and DG representations offers a way to reduce computational cost while retaining the generalized physics of the multi-fluid plasma model.

Acknowledgements

This material is based upon work supported by the Air Force Office of Scientific Research under award numbers FA9550-15-1-0271 and FA9550-14-1-0317.

References

[1] U. Shumlak, J. Loverich, Approximate Riemann solver for the two-fluid plasma model, J. Comput. Phys. 187 (2003) 620–638.
[2] B. Srinivasan, U. Shumlak, Analytical and computational study of the ideal full two-fluid plasma model and asymptotic approximations for Hall-magnetohydrodynamics, Phys. Plasmas (ISSN 1070-664X) 18 (9) (2011) 092113, http://dx.doi.org/10.1063/1.3640811.
[3] J.P. Freidberg, Ideal magnetohydrodynamic theory of magnetic fusion systems, Rev. Mod. Phys. 54 (3) (1982) 801–902.
[4] U. Shumlak, R. Lilly, N. Reddell, E. Sousa, B. Srinivasan, Advanced physics calculations using a multi-fluid plasma model, Comput. Phys. Commun. 182 (9) (2011) 1767–1770.
[5] E.T. Meier, U. Shumlak, A general nonlinear fluid model for reacting plasma-neutral mixtures, Phys. Plasmas 19 (7) (2012) 072508, http://link.aip.org/link/?PHP/19/072508/1.
[6] R.J. LeVeque, Finite Volume Methods for Hyperbolic Problems, 1st edn., Cambridge University Press, 2002.
[7] T. Barth, M. Ohlberger, Finite Volume Methods: Foundation and Analysis, John Wiley & Sons, Ltd, ISBN 9780470091357, 2004.
[8] P. Colella, M. Dorr, J. Hittinger, D. Martin, P. McCorquodale, High-order finite-volume adaptive methods on locally rectangular grids, J. Phys. 180 (2009) 012010.
[9] S.C. Jardin, A triangular finite element with first-derivative continuity applied to fusion MHD applications, J. Comput. Phys. 200 (1) (2004) 133–152.
[10] C. Sovinec, A. Glasser, T. Gianakon, D. Barnes, R. Nebel, S. Kruger, D. Schnack, S. Plimpton, A. Tarditi, M. Chu, Nonlinear magnetohydrodynamics simulation using high-order finite elements, J. Comput. Phys. 195 (1) (2004) 355–386.
[11] B. Cockburn, C.W. Shu, TVB Runge–Kutta local projection discontinuous Galerkin finite element for conservation laws II – general framework, Math. Comput. 52 (186) (1989) 411–435.
[12] F. Li, L. Xu, S. Yakovlev, Central discontinuous Galerkin methods for ideal MHD equations with the exactly divergence-free magnetic field, J. Comput. Phys. 230 (12) (2011) 4828–4847.
[13] V. Wheatley, H. Kumar, P. Huguenot, On the role of Riemann solvers in discontinuous Galerkin methods for magnetohydrodynamics, J. Comput. Phys. 229 (3) (2010) 660–680.
[14] B. Srinivasan, A. Hakim, U. Shumlak, Numerical methods for two-fluid dispersive fast MHD phenomena, Commun. Comput. Phys. 10 (1) (2011) 183–215.
[15] J.U. Brackbill, W.E. Pracht, An implicit, almost-Lagrangian algorithm for magnetohydrodynamics, J. Comput. Phys. 13 (1973) 455.
[16] R.E. Peterkin Jr., M.H. Frese, C.R. Sovinec, Transport of magnetic flux in an arbitrary coordinate ALE code, J. Comput. Phys. 140 (1) (1998) 148–171.
[17] U. Shumlak, T.W. Hussey, R.E. Peterkin Jr., Three-dimensional magnetic field enhancement in a liner implosion system, IEEE Trans. Plasma Sci. 23 (1) (1995) 83–88.
[18] A. Hakim, J. Loverich, U. Shumlak, A high resolution wave propagation scheme for ideal two-fluid plasma equations, J. Comput. Phys. 219 (2006) 418–442.
[19] N. Murphy, A. Young, C. Shen, J. Lin, L. Ni, The plasmoid instability during asymmetric inflow magnetic reconnection, Phys. Plasmas 20 (6) (2013) 061211.
[20] V.A. Izzo, Impurity mixing and radiation asymmetry in massive gas injection simulations of DIII-D, Phys. Plasmas 20 (5) (2013) 056107.
[21] J. Slough, R. Milroy, High flux FRC facility for stability and confinement studies, J. Fusion Energy 29 (6) (2010) 567–570.
[22] A.I. Macnab, S. Woodruff, Extended MHD simulations of the compression and stability of spheromaks for current drive, J. Fusion Energy 28 (2) (2009) 183–186.
[23] O.C. Zienkiewics, R.L. Taylor, P. Nithiarasu, The Finite Element Method for Fluid Dynamics, seventh edition, Elsevier, 2014.
[24] S. Jardin, J. Breslau, N. Ferraro, A high-order implicit finite element method for integrating the two-fluid magnetohydrodynamic equations in two dimensions, J. Comput. Phys. 226 (2) (2007) 2146–2174.
[25] L. Chacón, D. Knoll, J. Finn, An implicit, nonlinear reduced resistive MHD solver, J. Comput. Phys. 178 (1) (2002) 15–36.
[26] H.W. Reed, T.R. Hill, Triangular mesh methods for the neutron transport equation, Los Alamos Scientific Laboratory Report LA-UR-73-479, 1973.
[27] F. Bassi, S. Rebay, A high-order accurate discontinuous finite element method for the numerical solution of the compressible Navier–Stokes equations, J. Comput. Phys. 131 (1997) 267–279.
[28] F. Bassi, L. Botti, A. Colombo, S. Rebay, Agglomeration based discontinuous Galerkin discretization of the Euler and Navier–Stokes equations, Comput. Fluids 61 (2012) 77–85.
[29] E. Ferrer, R. Willden, A high-order discontinuous Galerkin finite element solver for the incompressible Navier–Stokes equations, Comput. Fluids 46 (1) (2011) 224–230.
[30] P. Birken, G. Gassner, M. Haas, C.-D. Munz, Preconditioning for modal discontinuous Galerkin methods for unsteady 3D Navier–Stokes equations, J. Comput. Phys. 240 (2013) 20–35.
[31] T. Warburton, G. Karniadakis, A discontinuous Galerkin method for the viscous MHD equations, J. Comput. Phys. (ISSN 0021-9991) 152 (2) (1999) 608–641.
[32] J.A. Rossmanith, D.C. Seal, A positivity-preserving high-order semi-Lagrangian discontinuous Galerkin scheme for the Vlasov–Poisson equations, J. Comput. Phys. 230 (16) (2011) 6203–6232.
[33] B. Cockburn, C.W. Shu, Runge–Kutta discontinuous Galerkin methods for convection-dominated problems, J. Sci. Comput. 16 (3) (2001) 173–261.
[34] U. Shumlak, R. Lilly, N. Reddell, E. Sousa, B. Srinivasan, Advanced physics calculations using a multi-fluid plasma model, Comput. Phys. Commun. 18 (2011) 1767–1770.
[35] B. Srinivasan, Numerical methods for 3-dimensional magnetic confinement configurations using two-fluid plasma equations, Ph.D. thesis, University of Washington, 2010.
[36] U. Ascher, S. Ruuth, R. Spiteri, Implicit–explicit Runge–Kutta methods for time-dependent partial differential equations, Appl. Numer. Math. 25 (1997) 151–167.
[37] A. Kanevsky, M. Carpenter, D. Gottlieb, J. Hesthaven, Application of implicit–explicit high order Runge–Kutta methods to discontinuous-Galerkin schemes, J. Comput. Phys. 225 (2007) 1753–1781.
[38] M.G. Haines, A review of the dense Z-pinch, Plasma Phys. Control. Fusion 53 (9) (2011) 093001.
[39] S. Hirshman, D. Sigmar, Neoclassical transport of impurities in tokamak plasmas, Nucl. Fusion 21 (9) (1981) 1079.

[40] P. Helander, C.D. Beidler, T.M. Bird, M. Drevlak, Y. Feng, R. Hatzky, F. Jenko, R. Kleiber, J.H.E. Proll, Y. Turkin, P. Xanthopoulos, Stellarator and tokamak plasmas: a comparison, Plasma Phys. Control. Fusion 54 (12) (2012) 124009.
[41] J.D. Lindl, P. Amendt, R.L. Berger, S.G. Glendinning, S.H. Glenzer, S.W. Haan, R.L. Kauffman, O.L. Landen, L.J. Suter, The physics basis for ignition using indirect-drive targets on the National Ignition Facility, Phys. Plasmas 11 (2004) 339.
[42] C. Bellei, P.A. Amendt, S.C. Wilks, M.G. Haines, D.T. Casey, C.K. Li, R. Petrasso, D.R. Welch, Species separation in inertial confinement fusion fuels, Phys. Plasmas 20 (2013) 012701.
[43] C. Munz, P. Omnes, R. Schneider, E. Sonnendruer, U. Voss, Divergence correction techniques for Maxwell solvers based in a hyperbolic model, J. Comput. Phys. 161 (2000) 484–511.
[44] E.M. Sousa, A blended finite element method for multi-fluid plasma modeling, Ph.D. thesis, University of Washington, Seattle, WA 98195, 2014.
[45] J.N. Reddy, An Introduction to the Finite Element Method, 3rd edn., McGraw-Hill, 2006.
[46] D.F. Griffiths, D.J. Higham, Numerical Methods for Ordinary Differential Equations, Springer, 2010.
[47] J. Crank, P. Nicolson, A partial method for numerical evaluation of solutions of partial differential equations of the heat-conduction type, Adv. Comput. Math. 6 (1996) 207–226.
[48] T.J. Ypma, Historical development of the Newton–Raphson method, SIAM Rev. 37 (4) (1995) 531–551.
[49] J. Loverich, U. Shumlak, A discontinuous Galerkin method for the full two-fluid plasma model, Comput. Phys. Commun. (ISSN 0010-4655) 169 (1–3) (2005) 251–255, http://www.sciencedirect.com/science/article/B6TJ5-4FWV2KT-5/2/e932f6ea4ea9a11dfad06528fb6b71f0.
[50] J. Loverich, A. Hakim, U. Shumlak, A discontinuous Galerkin method for ideal two-fluid plasma equations, Commun. Comput. Phys. 9 (2) (2011) 240–268.
[51] P.L. Roe, Approximate Riemann solvers, parameter vectors and difference schemes, J. Comput. Phys. 43 (1981) 357.
[52] J.S. Hesthaven, T. Warburton, Nodal Discontinuous Galerkin Methods: Algorithms, Analysis, and Applications, Springer, 2008.
[53] S. Baboolal, Finite-difference modeling of solitons induced by a density hump in a plasma multi-fluid, Math. Comput. Simul. 55 (2001) 309–316.
[54] J. Birn, J.F. Drake, M.A. Shay, B.N. Rogers, R.E. Denton, M. Hesse, M. Kuznetsova, Z.W. Ma, A. Bhattacharjee, A. Otto, P.L. Pritchett, Geospace Environmental Modeling (GEM) magnetic reconnection challenge, J. Geophys. Res. 106 (A3) (2001) 3715–3719.
[55] M. Brio, C.C. Wu, An upwind differencing scheme for the equations of ideal magnetohydrodynamics, J. Comput. Phys. 75 (1988) 400–422.
[56] P. Amendt, S.C. Wilks, C. Bellei, C.K. Li, R.D. Petrasso, The potential role of electric fields and plasma barodiffusion on the inertial confinement fusion database, Phys. Plasmas 18 (2011) 056308.
[57] D.T. Casey, J.A. Frenje, M.G. Johnson, M.J.E. Manuel, H.G. Rinderknecht, N. Sinenian, F.H. Séguin, C.K. Li, R.D. Petrasso, P.B. Radha, J.A. Delettrez, V.Y. Glebov, D.D. Meyerhofer, T.C. Sangster, D.P. McNabb, P.A. Amendt, R.N. Boyd, J.R. Rygg, H.W. Herrmann, Y.H. Kim, A.D. Bacher, Evidence for stratification of deuterium-tritium fuel in inertial confinement fusion implosions, Phys. Rev. Lett. 108 (2012) 075002.